

Non-Radial Oscillation Modes in Hybrid Stars with Hyperons and Delta Baryons: Full General Relativity Formalism vs. Cowling Approximation

Ishfaq Ahmad Rather ^{1,*}, Kau D. Marquez ^{2,†}, Prashant Thakur ^{3,‡} and Odilon Lourenço ^{2,§}

¹*Institut für Theoretische Physik, Goethe Universität,
Max-von-Laue-Str. 1, D-60438 Frankfurt am Main, Germany*

²*Departamento de Física e Laboratório de Computação Científica Avançada e Modelamento (Lab-CCAM),
Instituto Tecnológico de Aeronáutica, DCTA, 12228-900 São José dos Campos/SP, Brazil*

³*Department of Physics, BITS-Pilani, K. K. Birla Goa Campus, 403726 Goa, India*

We study the effects of hyperons, delta baryons, and quark matter phase transitions on f -mode oscillations in neutron stars. Using the density-dependent relativistic mean-field model (DDME2) for the hadronic phase and the density-dependent quark mass (DDQM) model for the quark phase, we construct hadronic and hybrid equations of state (EoSs) consistent with astrophysical constraints. Including hyperons and delta baryons soften the EoS, reducing maximum mass, while phase transition to the quark matter further softens the EoS, decreasing the speed of sound and hence the maximum mass. f -mode frequencies, calculated using both the Cowling approximation and the general relativistic (GR) frameworks, reveal a significant overestimation by the Cowling method of about 10–30%, with discrepancies decreasing for more massive stars. We derive universal relations connecting the frequencies of the f -mode to the average density, compactness, and tidal deformability, finding significant deviations due to hyperons and delta baryons. Empirical relations for mass-scaled and radius-scaled frequencies are also provided, highlighting the importance of GR calculations for accurate modeling. These findings highlight the potential of gravitational wave asteroseismology to constrain neutron star EoSs and internal structure.

I. INTRODUCTION

In recent years, our understanding of the universe has expanded as we now observe astronomical events through multiple signals: electromagnetic waves, gravitational waves, neutrinos, and cosmic rays. This new era of multi-messenger astronomy enables a more comprehensive view of phenomena like neutron star mergers, providing unprecedented insights into the properties of dense matter. Neutron star (NS) asteroseismology, in particular, has emerged as a crucial tool for probing the dense matter equation of state (EoS), especially as gravitational wave detections grow in number and precision. Landmark events such as GW170817 [1, 2] and GW190425 [3] have already provided valuable EoS constraints, while upcoming facilities like LIGO-Virgo-KAGRA, the Einstein Telescope [4–6] and the Cosmic Explorer are set to push these limits even further.

The EoS that governs nuclear matter at the extreme densities attained inside NSs is central to determining their macroscopic structure and properties. Though NSs are largely composed of neutrons, a small but crucial fraction of protons, leptons, and possibly other particles is also present in their interiors. These degrees of freedom appear to maintain the stability of nuclear matter under chemical equilibrium and charge neutrality conditions, as well as due to energetic considerations, and are very contingent on the dense matter model adopted. However, much remains unknown about the EoS and the

exact composition of NS interiors due to the complexity of strong interactions, especially at high densities beyond the nuclear saturation density (n_0). At densities surpassing several times n_0 , exotic particles beyond the usual nucleons (neutrons and protons) are expected to appear. Most theoretical models predict that NS matter could comprise the entire spin-1/2 baryon octet, including the hyperons. One must observe that the inclusion of hyperons in the EoS, while energetically favorable, has sparked the so-called “hyperon puzzle”: hyperons soften the EoS, reducing the maximum mass an NS can achieve and potentially conflicting with observations of massive NSs [7]. To address more exotic degrees of freedom, researchers have also considered other particles like kaons and spin-3/2 baryons within relativistic mean-field models. Delta (Δ) baryons, for example, are about 30 % heavier than nucleons (with a mass of around 1232 MeV) and are expected to appear at similar densities to hyperons, in the range of $2-3n_0$ [8, 9]. Studies suggest that with appropriate coupling strengths, delta baryons could indeed make up a significant fraction of NS matter, potentially impacting the EoS and other NS properties [10]. At even higher densities, a phase transition from hadronic matter to deconfined quark matter may occur, resulting in a hybrid star structure with a quark core surrounded by a hadronic shell. This hadron-quark deconfinement transition is a key prediction of quantum chromodynamics (QCD) at extreme densities [1, 11].

Understanding neutron star oscillation modes has gained increased attention due to recent advancements in multi-messenger astronomy. Gravitational wave observatories, such as LIGO and Virgo, have opened new possibilities for detecting the subtle spacetime ripples generated by these oscillations, especially following neutron star mergers. These observations complement electromag-

* rather@astro.uni-frankfurt.de

† kau@ita.br

‡ p20190072@goa.bits-pilani.ac.in

§ odilon.ita@gmail.com

netic data from X-ray and radio telescopes, potentially allowing for constraints on neutron star models through observed mode frequencies, damping times, and mode couplings. Each type of mode interacts distinctly with the neutron star’s dense matter properties, making them sensitive probes of the EoS and phase transitions, such as the potential appearance of hyperons or deconfined quarks in the stellar core. Hence, by analyzing oscillation modes, one can extract information on the internal structure and composition of neutron stars. These oscillation modes effectively act as a spectral fingerprint of the star’s static properties, offering a seismological approach to probe otherwise inaccessible regions of dense nuclear matter. Small deviations in static properties, such as the appearance of exotic phases (e.g., hyperons or quark matter) or changes in the crust composition, can lead to measurable shifts in mode frequencies and damping rates, making them highly sensitive to the nature of matter at extreme densities.

When an NS is mechanically perturbed, it exhibits oscillation behaviors that can be classified into radial and non-radial modes. Radial oscillations involve uniform expansion and contraction while maintaining the star’s spherical shape, showing two classes of behavior based on whether they are localized in the dense core or the lower-density outer envelope of the star. These two regions are separated by a “wall” in the adiabatic index at the neutron drip point, that is universally tied to the neutron drip density common to all realistic EoS models [12]. Although radial modes do not directly emit gravitational waves (GWs), they can interact with non-radial modes, enhancing GW signals [13, 14]. For instance, in the post-merger phase of a binary NS collision, a hyper-massive NS may emit GWs at high frequencies (1–4 kHz), which are potentially detectable [15].

In contrast, non-radial oscillations – as f -modes, associated with fluid oscillations; g -modes, driven by compositional gradients; and p -modes, which reflect pressure-driven oscillations – cause distortions due to forces like pressure and buoyancy [16]. Gravitational perturbations in spherically symmetric stars are categorized as polar or axial. Polar perturbations lead to the f , p , and g modes, while axial perturbations result in the r and w modes. In non-rotating stars, these perturbations are entirely independent [17]. Among non-radial modes, the f -mode is particularly significant as it emits detectable GWs. Advanced detectors like the Einstein Telescope and Cosmic Explorer, and possibly even current detectors such as LIGO/Virgo/KAGRA, are expected to observe these signals [4–6, 18, 19]. The f -mode frequency is closely tied to tidal deformability during the inspiral phase of NS mergers, as fluid perturbations peak at the stellar surface, strongly coupling to the tidal field. Apart from neutron star mergers various phenomena can trigger the excitation of f -modes in neutron stars, including the formation of newly born neutron stars [20], starquakes [21, 22], magnetar activity [23, 24]. For GW170817, the 90% credible interval for the f -mode frequency was estimated between 1.43 kHz and 2.90 kHz for the more massive NS and 1.48 kHz and 3.18 kHz for the less massive one [25].

Additionally, the f -mode relates to NS properties like compactness [26], moment of inertia [27], and static tidal polarizability [28]. These relations are universal, applying even to quark stars without crusts or hybrid stars with first-order transitions [29].

The study of the f -mode is often conducted using the Cowling approximation instead of a full general relativistic (GR) framework. In the Cowling approximation, gravitational potential perturbations are neglected, focusing solely on fluid perturbations. This simplification aids calculations but introduces an error of about 10–30% in the f -mode frequency [25, 30]. On the other hand, the full GR framework incorporates both fluid and metric perturbations, comprehensively addressing the limitations of the Cowling approximation. The Cowling approximation neglects metric perturbations, leading to smaller errors for neutron stars with higher masses. This is because massive neutron stars have fluid perturbations that peak more strongly near the surface, while their weaker core coupling to metric perturbations reduces the impact of these neglected terms. Consequently, the relative error between the Cowling approximation and the full GR framework decreases as the mass of the neutron star increases. Several studies have explored the f -mode oscillations of neutron stars under the Cowling approximation, considering nucleonic and hyperonic compositions [30–32], hybrid stars [33], and scenarios involving dark matter [34–36]. However, some research emphasizes the need for a full General Relativity (GR) treatment to achieve greater accuracy [25, 29, 31, 37, 38]. In this study, both methodologies will be applied allowing to a precise evaluation of the method discrepancies.

This study examines the non-radial oscillation modes of NSs with various matter compositions, including nucleonic stars with Δ -admixed matter and hyperon stars containing Δ baryons. For the first time, the analysis considers these compositions in scenarios where a hadron-quark phase transition occurs within the star. While previous research has focused on radial oscillations in NSs along with exotic phases, such as dark matter and deconfined quark matter [39–46], this work extends the exploration to non-radial modes under similar conditions. The paper is organized as follows: Sec II provides the description of the NS used in this study. Sec II.1 outlines the EoS for the DD-RMF model with Δ baryons, the quark matter EoS, and the construction of the hybrid EoS. Sec II.2 discusses the Tolman-Oppenheimer-Volkoff (TOV) equations governing NS structure. Sec III details the non-radial oscillation analysis within both full GR formalism and the Cowling approximation. Sec IV presents the EoS and stellar properties, such as the speed of sound and mass-radius profiles for various compositions, with and without phase transitions. Sec IV.2 examines the f -mode frequency as a function of stellar properties in both the Cowling and GR frameworks. Sec V introduces empirical fits and universal relations between the f -mode frequency and other key parameters. Finally, Sec VI provides our concluding remarks.

II. NEUTRON STAR DESCRIPTION

II.1. Microphysics

II.1.1. Hadronic matter

In this study, we describe the hadronic matter inside neutron stars using a density-dependent relativistic mean-field (DD-RMF) approach. This model is known for accurately reproducing experimental properties of nuclear matter and remains consistent with astrophysical con-

straints [47–49]. The interaction framework considers nucleons and other hadrons interacting via the exchange of virtual mesons. Specifically, the DD-RMF model used here includes the scalar meson σ , the vector mesons ω and ϕ (with hidden strangeness), and the isovector-vector meson ρ .

The Lagrangian density serves as the foundational ansatz in any RMF theory, incorporating contributions from free baryons and mesons as well as interaction terms between them. In the mean-field approximation, the Lagrangian of the relativistic model used here to describe hadronic interactions is given by

$$\begin{aligned} \mathcal{L}_{\text{RMF}} = & \sum_{b \in H} \bar{\psi}_b \left[i\gamma^\mu \partial_\mu - \gamma^0 (g_{\omega b} \omega_0 + g_{\phi b} \phi_0 + g_{\rho b} I_{3b} \rho_{03}) - (m_b - g_{\sigma b} \sigma_0) \right] \psi_b \\ & - \frac{i}{2} \sum_{b \in \Delta} \bar{\psi}_{b\mu} \left[\varepsilon^{\mu\nu\rho\lambda} \gamma_5 \gamma_\nu \partial_\rho - \gamma^0 (g_{\omega b} \omega_0 + g_{\rho b} I_{3b} \rho_{03}) - (m_b - g_{\sigma b} \sigma_0) \zeta^{\mu\lambda} \right] \psi_{b\nu} \\ & + \sum_{\lambda} \bar{\psi}_\lambda (i\gamma^\mu \partial_\mu - m_\lambda) \psi_\lambda - \frac{1}{2} m_\sigma^2 \sigma_0^2 + \frac{1}{2} m_\omega^2 \omega_0^2 + \frac{1}{2} m_\phi^2 \phi_0^2 + \frac{1}{2} m_\rho^2 \rho_{03}^2 \end{aligned} \quad (1)$$

where the first sum represents the Dirac-type interacting Lagrangian for the spin-1/2 baryon octet ($H = \{n, p, \Lambda, \Sigma^-, \Sigma^0, \Sigma^+, \Xi^-, \Xi^0\}$) and the second sum represents the Rarita-Schwinger interacting Lagrangian for the particles of the spin-3/2 baryon decuplet ($\Delta = \{\Delta^-, \Delta^0, \Delta^+, \Delta^{++}\}$), where $\varepsilon^{\mu\nu\rho\lambda}$ is the Levi-Civita symbol, $\gamma_5 = i\gamma_0\gamma_1\gamma_2\gamma_3$ and $\zeta^{\mu\lambda} = \frac{i}{2} [\gamma^\mu, \gamma^\lambda]$. We note that spin-3/2 baryons are described by the Rarita-Schwinger Lagrangian density, where their vector-valued spinor has additional components compared to the four components in spin-1/2 Dirac spinors. However, as shown in [50], the equations of motion for spin-3/2 particles can be simplified and written in a form analogous to those for spin-1/2 particles within the RMF framework. The last sum describes the leptons admixed in the hadronic matter as a free non-interacting fermion gas ($\lambda = \{e, \mu\}$), as their inclusion is necessary in order to ensure the β -equilibrium and charge neutrality essential to stellar matter. The remaining terms account for the purely mesonic part of the Lagrangian.

In DD-RMF models, coupling constants are typically functions of either the scalar density n_s or the vector density n_B . Most commonly, vector density parameterizations are used, as they influence only the self-energy rather than the total energy [52]. Here, we adopt the DD-RMF parametrization known as DDME2 [53], where meson couplings scale with the baryonic density factor $\eta = n_B/n_0$ obeying the function

$$g_{ib}(n_B) = g_{ib}(n_0) \frac{a_i + b_i(\eta + d_i)^2}{a_i + c_i(\eta + d_i)^2} \quad (2)$$

for $i = \sigma, \omega, \phi$ and

$$g_{\rho b}(n_B) = g_{\rho b}(n_0) \exp[-a_\rho(\eta - 1)], \quad (3)$$

TABLE I. DDME2 parameters (top) and its predictions to the nuclear matter at saturation density (bottom).

i	m_i (MeV)	a_i	b_i	c_i	d_i	$g_{iN}(n_0)$
σ	550.1238	1.3881	1.0943	1.7057	0.4421	10.5396
ω	783	1.3892	0.9240	1.4620	0.4775	13.0189
ρ	763	0.5647	—	—	—	7.3672

Quantity	Constraints [47, 51]	This model
n_0 (fm^{-3})	0.148–0.170	0.152
$-B/A$ (MeV)	15.8–16.5	16.14
K_0 (MeV)	220–260	252
S_0 (MeV)	31.2–35.0	32.3
L_0 (MeV)	38–67	51

for $i = \rho$.

The model parameters are fitted to binding energies, charge radii, and differences between neutron and proton radii of spherical nuclei, as well as some bulk parameters related to infinite and pure nucleonic matter at n_0 , namely, the saturation density itself, binding energy (B/A), incompressibility (K_0), and symmetry energy (S_0). All of them are shown in Table I, along with the value of the symmetry energy slope at n_0 (L_0). In order to determine the meson couplings to other hadronic species, we define the ratio of the baryon coupling to the nucleon one as $\chi_{ib} = g_{ib}/g_{iN}$, with $i = \{\sigma, \omega, \phi, \rho\}$. In this work, we consider hyperons and/or deltas admixed in the nucleonic matter and follow the proposal of [54] to determine their respective χ_{ib} ratios. This calibration follows a unified approach based on symmetry principles, particularly the requirement that the Yukawa coupling terms in the Lagrangian density of DD-RMF models remain invariant

under SU(3) and SU(6) group transformations. Hence, the couplings can be fixed to reproduce the potentials $U_\Lambda = -28$ MeV, $U_\Sigma = 30$ MeV, $U_\Xi = -4$ MeV and $U_\Delta = -98$ MeV in terms of a single free parameter α_V . Our choice of $\alpha_V = 1.0$ for the baryon-meson coupling scheme corresponds to an unbroken SU(6) symmetry, and the values of χ_{ib} are shown in Table II taking into account the isospin projections in the Lagrangian terms [55].

TABLE II. Baryon-meson coupling constants χ_{ib} [54].

b	$\chi_{\omega b}$	$\chi_{\sigma b}$	$I_{3b}\chi_{\rho b}$	$\chi_{\phi b}$
Λ	2/3	0.611	0	0.471
$\Sigma^-, \Sigma^0, \Sigma^+$	2/3	0.467	-1, 0, 1	-0.471
Ξ^-, Ξ^0	1/3	0.284	-1/2, 1/2	-0.314
$\Delta^-, \Delta^0, \Delta^+, \Delta^{++}$	1	1.053	-3/2, -1/2, 1/2, 3/2	0

From the Lagrangian (1), thermodynamic quantities can be calculated in the standard way for RMF models. The baryonic and scalar densities of a baryon of the species b are given, respectively, by

$$n_b = \frac{\lambda_b}{2\pi^2} \int_0^{k_{Fb}} dk k^2 = \frac{\lambda_b}{6\pi^2} k_{Fb}^3, \quad (4)$$

and

$$n_b^s = \frac{\lambda_b}{2\pi^2} \int_0^{k_{Fb}} dk \frac{k^2 m_b^*}{\sqrt{k^2 + m_b^{*2}}}, \quad (5)$$

with k_F denoting the Fermi momentum, since we assume the stellar matter to be at zero temperature, and λ_b is the spin degeneracy factor (2 for the baryon octet and 4 for the delta resonances). The effective masses are

$$m_b^* = m_b - g_{\sigma b}\sigma_0. \quad (6)$$

The energy density is given by

$$\begin{aligned} \varepsilon_B = & \sum_b \frac{\gamma_b}{2\pi^2} \int_0^{k_{Fb}} dk k^2 \sqrt{k^2 + m_b^{*2}} \\ & + \sum_\lambda \frac{1}{\pi^2} \int_0^{k_{F\lambda}} dk k^2 \sqrt{k^2 + m_\lambda^2} \\ & + \frac{m_\sigma^2}{2} \sigma_0^2 + \frac{m_\omega^2}{2} \omega_0^2 + \frac{m_\phi^2}{2} \phi_0^2 + \frac{m_\rho^2}{2} \rho_{03}^2. \end{aligned} \quad (7)$$

The effective chemical potentials read

$$\mu_b^* = \mu_b - g_{\omega b}\omega_0 - g_{\rho b}I_{3b}\rho_{03} - g_{\phi b}\phi_0 - \Sigma^r, \quad (8)$$

where Σ^r is the rearrangement term, necessary to ensure thermodynamical consistency due to the density-dependent couplings,

$$\begin{aligned} \Sigma^r = & \sum_b \left[\frac{\partial g_{\omega b}}{\partial n_b} \omega_0 n_b + \frac{\partial g_{\rho b}}{\partial n_b} \rho_{03} I_{3b} n_b + \frac{\partial g_{\phi b}}{\partial n_b} \phi_0 n_b \right. \\ & \left. - \frac{\partial g_{\sigma b}}{\partial n_b} \sigma_0 n_b^s \right], \end{aligned} \quad (9)$$

and the μ_b are determined by the chemical equilibrium condition

$$\mu_b = \mu_n - q_b \mu_e, \quad (10)$$

in terms of the chemical potential of the neutron and the electron, with $\mu_\mu = \mu_e$. The particle populations of each individual species are determined by Eq. (10) together with the charge neutrality condition $\sum_i n_i q_i = 0$, where q_i is the charge of the baryon or lepton i . The pressure, finally, is given by

$$P = \sum_i \mu_i n_i - \epsilon + n_B \Sigma^r, \quad (11)$$

which receives a correction from the rearrangement term to guarantee thermodynamic consistency and energy-momentum conservation [56, 57]. In the above expression, ϵ is the total energy density including leptons.

II.1.2. Deconfined quark matter

In this study, we adopt the density-dependent quark mass (DDQM) model [58] to describe quark matter, a simple and versatile framework well-suited for investigating the deconfinement phase transition in hybrid stars [59]. The DDQM model simulates the QCD quark confinement through density-dependent quark masses defined by

$$m_i = m_{i0} + \frac{D}{n_B^{1/3}} + C n_B^{1/3} = m_{i0} + m_I, \quad (12)$$

where m_{i0} ($i = u, d, s$) is the current mass of the i th quark, n_B is the baryon number density and m_I is the density-dependent term that encompasses the interaction between quarks. This model-free parameters C and D dictate linear confinement and the leading-order perturbative interactions, respectively [58].

Introducing density dependence for state variables, such as density, temperature, or magnetic field, requires careful handling to maintain thermodynamic consistency, analogous to the approach in Eq. (9) for the DD-RMF model. We follow the formalism in [58], which ensures thermodynamic consistency in DDQM. At zero temperature, the fundamental differential relation for energy density reads

$$d\varepsilon = \sum_i \mu_i^* dn_i, \quad (13)$$

where ε is the matter contribution to the energy density of the system, μ_i are the particle chemical potentials and n_i are the particle densities.

To express this model in terms of effective chemical potentials, we represent the energy density as for a free system as

$$\varepsilon = \Omega_0(\{\mu_i^*\}, \{m_i\}) + \sum_i \mu_i^* n_i, \quad (14)$$

using density-dependent quark masses $m_i(n_B)$ and effective chemical potentials μ_i^* , where Ω_0 is the thermodynamic potential of a free system. We can differentiate this form to yield

$$d\varepsilon = d\Omega_0 + \sum_i \mu_i^* dn_i + \sum_i n_i d\mu_i^*. \quad (15)$$

Explicitly, we can write $d\Omega_0$ as

$$d\Omega_0 = \sum_i \frac{\partial \Omega_0}{\partial \mu_i^*} d\mu_i^* + \sum_i \frac{\partial \Omega_0}{\partial m_i} dm_i, \quad (16)$$

with

$$dm_i = \sum_j \frac{\partial m_i}{\partial n_j} dn_j, \quad (17)$$

where, to ensure thermodynamic consistency, the densities are connected to the effective chemical potentials by

$$n_i = -\frac{\partial \Omega_0}{\partial \mu_i^*}. \quad (18)$$

Eq. (15) can then be rewritten as

$$d\varepsilon = \sum_i \left(\mu_i^* + \sum_j \frac{\partial \Omega_0}{\partial m_j} \frac{\partial m_j}{\partial n_i} \right) dn_i, \quad (19)$$

providing a relation between the real and effective chemical potentials,

$$\mu_i = \mu_i^* + \sum_j \frac{\partial \Omega_0}{\partial m_j} \frac{\partial m_j}{\partial n_i}. \quad (20)$$

Consequently, from the fundamental relation $P = -\varepsilon + \sum_i \mu_i n_i$, the pressure P is given by

$$P = -\Omega_0 + \sum_{i,j} \frac{\partial \Omega_0}{\partial m_j} n_i \frac{\partial m_j}{\partial n_i}, \quad (21)$$

yielding a thermodynamically consistent EoS for quark matter.

The EoS for the quark model is derived using experimentally consistent quark masses and selected parameters suited for hybrid stars based on phase coexistence with various hadronic configurations. The transition point between phases is highly sensitive to the free parameters of the DDQM model, which lacks strong empirical constraints. Therefore, parameter selection often involves considering the stability window under the Bodmer-Witten hypothesis [60, 61], which posits that strange quark matter – comprising roughly equal amounts of u , d , and s quarks – could be more stable than hadronic matter. If true, neutron stars could convert entirely into strange stars. However, since our focus is on hybrid stars, we exclude parameter sets that satisfy this hypothesis. Additionally, studies have shown that for high values of the C parameter, the surface density of strange stars can approach or fall below nuclear saturation density, indicating

a possible phase transition. Such parameters also result in hybrid star phase transitions at densities above nuclear saturation and yield strange stars with masses around $2 M_\odot$. Ref. [62] provides a detailed analysis of how DDQM parameters affect strange matter stability, and the specific choice of the quark matter-free parameters C and D adopted here is discussed in detail in Ref. [40].

II.1.3. Phase transition and hybrid EoS construction

Studying matter under extreme conditions is inherently difficult due to the complexity of QCD. The two main theoretical approaches – lattice QCD (LQCD) and effective models – each have significant limitations. LQCD faces challenges such as the sign problem, computational constraints, and limited applicability at high chemical potentials, making it ineffective for mapping the QCD phase diagram in these regimes (see [63]). Consequently, effective models are often employed, particularly in the context of compact objects like neutron stars.

A longstanding tension exists between LQCD and effective models regarding the nature of the QCD phase transition. LQCD indicates a smooth crossover around 160–170 MeV at low chemical potentials [64, 65], while effective models predict a first-order transition at high densities. This transition is expected to culminate in a critical endpoint (CEP), beyond which it becomes second-order. However, the existence and precise location of the CEP remain uncertain [66, 67]. For example, [68] suggests that at zero temperature, the transition onset requires a chemical potential exceeding 1050 MeV in the Polyakov loop formalism.

The characteristics of the transition vary according to the quark and hadron EoS models employed. In this study, we assume that the hadron-quark deconfinement transition is a first-order phase transition, as predicted by effective models in the high-density region of the QCD phase diagram. A phase transition can occur as either a Maxwell or a mixed phase (also called Gibbs) transition. In a Maxwell transition, the phases remain separate and maintain local charge conservation, whereas, in a mixed transition, quarks and hadrons coexist over a range of baryonic densities with global charge conservation. The hadron-quark phase surface tension serves as the primary criterion for determining the type of phase transition. Values above 60 MeV/fm² favor a Maxwell transition [69, 70], while lower values suggest a mixed transition. Given the uncertainties in surface tension estimates [71–74]. The thermodynamic description of this process involves matching the EoS of the two phases and identifying the point of phase coexistence.

In this study, we apply the Maxwell construction, producing a hybrid EoS with a first-order phase transition at critical values of baryonic chemical potential and pressure. According to Gibbs' criteria, the transition occurs at the

point where

$$P^{(i)} = P^{(f)} = P_0, \quad (22)$$

$$\mu^{(i)}(P_0) = \mu^{(f)}(P_0) = \mu_0, \quad (23)$$

sets the transition between the initial (i) and final (f) homogeneous phases, both at $T = 0$ MeV, with

$$\mu^{(i,f)} = \frac{\varepsilon^{(i,f)} + P^{(i,f)}}{n_B^{(i,f)}}, \quad (24)$$

where $\varepsilon^{(i,f)}$, $P^{(i,f)}$ and $n_B^{(i,f)}$ are the total energy density, pressure, and baryon number density, obtained from the EoS of each phase. The conditions above the values of P_0 and μ_0 are to be determined from the equations of state of both hadronic and deconfined quark phases. The transition point location, for a given baryonic composition in the hadronic phase, will be notably influenced by the choice of the free parameters for the DDQM model [59].

II.2. Macrophysics

Moving from micro to macrophysics involves applying the EoS for the dense matter to conditions of mechanical (or hydrostatic) equilibrium, as NS is assumed to have stable internal structures. The intense gravitational field of NS makes their structure and dynamical evolution be governed by Einstein's equations of General Relativity,

$$G_{\mu\nu} = R_{\mu\nu} - \frac{1}{2}Rg_{\mu\nu} = 8\pi T_{\mu\nu}, \quad (25)$$

where $R_{\mu\nu}$ is the Ricci tensor and R is the Ricci scalar, and $T_{\mu\nu}$ is the energy-momentum tensor.

One can obtain the Tolman-Oppenheimer-Volkoff (TOV) equations [75, 76] for the equilibrium structure of NSs by solving the Einstein field equation with the below-defined metric,

$$\frac{dP(r)}{dr} = -\frac{[\varepsilon(r) + P(r)][m(r) + 4\pi r^3 P(r)]}{r^2(1 - 2m(r)/r)}, \quad (26)$$

$$\frac{dm(r)}{dr} = 4\pi r^2 \varepsilon(r), \quad (27)$$

by taking the $T_{\mu\nu}$ of an homogeneous fluid,

$$T_{\mu\nu} = Pg_{\mu\nu} + (P + \varepsilon)u_\mu u_\nu, \quad (28)$$

where $g_{\mu\nu}$ is the metric tensor, P is the pressure, ε is the energy density, and u_μ is the four-velocity, and considering static spherically symmetric stars, described by the Schwarzschild metric as [77]

$$ds^2 = e^{\nu(r)} dt^2 - e^{\lambda(r)} dr^2 - r^2(d\theta^2 + \sin^2\theta d\phi^2), \quad (29)$$

where $e^{\nu(r)}$ and $e^{\lambda(r)}$ are the metric functions.

Using the given EoS, the TOV Eqs. (26)-(27) are solved with initial conditions $m(r=0) = 0$ and $P(r=0) = P_c$, where P_c represents the central pressure. The star's radius, R , is defined where the pressure vanishes at the surface, $P(R) = 0$, and the total mass is then given by $M = m(R)$.

III. OSCILLATION MODES

III.1. Non-radial oscillations in general relativity

To determine the frequencies of the f -modes in the full general relativity formalism, we solve Einstein's field equations assuming that the gravitational waves represent perturbations to the static background spacetime metric of a non-rotating neutron star. The perturbed metric is given by

$$g_{\mu\nu} = g_{\mu\nu}^0 + h_{\mu\nu}, \quad (30)$$

Only even-parity perturbations of the Regge-Wheeler metric are significant in this context [78]. A small perturbation, $h_{\mu\nu}$, is introduced to a static, spherically symmetric background metric, which is described as:

$$\begin{aligned} ds^2 = & -e^{\nu(r)}[1 + r^l H_0(r)e^{i\omega t} Y_{lm}(\phi, \theta)]c^2 dt^2 \\ & + e^{\lambda(r)}[1 - r^l H_0(r)e^{i\omega t} Y_{lm}(\phi, \theta)]dr^2 \\ & + [1 - r^l K(r)e^{i\omega t} Y_{lm}(\phi, \theta)]r^2 d\Omega^2 \\ & - 2i\omega r^{l+1} H_1(r)e^{i\omega t} Y_{lm}(\phi, \theta) dt dr, \end{aligned} \quad (31)$$

where, H_0 , H_1 , and K represent the radial perturbations of the metric, while the angular dependence is captured by the spherical harmonics Y_l^m . The time dependence of the perturbed metric components can be expressed using the factor $e^{i\omega t}$ for a wave mode. Here ω is a complex quantity, as the waves decay due to the imposed open boundary conditions. The real part of ω represents the oscillation frequency, while the imaginary part corresponds to the inverse of the wave mode's gravitational wave damping time (positive).

The perturbations of the energy-momentum tensor of the fluid must also be considered in the Einstein equations. The components of the Lagrangian displacement vector $\xi^a(r, \theta, \phi)$ describe the perturbations of the fluid within the star:

$$\begin{aligned} \xi^r &= r^{l-1} e^{-\frac{\lambda}{2}} W Y_m^l e^{i\omega t}, \\ \xi^\theta &= -r^{l-2} V \partial_\theta Y_m^l e^{i\omega t}, \\ \xi^\phi &= -\frac{r^{l-2}}{\sin^2\theta} V \partial_\phi Y_m^l e^{i\omega t}. \end{aligned} \quad (32)$$

here, W and V are functions of r that represent fluid perturbations confined to the star's interior.

The gravitational wave equations can then be written as a set of four coupled linear differential equations for the four perturbation functions, H_1 , K , W , and X , which do

not diverge inside the star for any given value of ω . [79, 80],

$$r \frac{dH_1}{dr} = -[l + 1 + 2be^\lambda + 4\pi r^2 e^\lambda (p - \varepsilon)]H_1 + e^\lambda [H_0 + K - 16\pi(\varepsilon + p)V], \quad (33)$$

$$r \frac{dK}{dr} = H_0 + (n_l + 1)H_1 + [e^\lambda Q - l - 1]K - 8\pi(\varepsilon + p)e^{\lambda/2}W, \quad (34)$$

$$r \frac{dW}{dr} = -(l + 1)[W + le^{\frac{\lambda}{2}}V] + r^2 e^{\lambda/2} \left[\frac{e^{-\nu/2}X}{(\varepsilon + p)c_{\text{ad}}^2} + \frac{H_0}{2} + K \right], \quad (35)$$

$$\begin{aligned} r \frac{dX}{dr} = & -lX + \frac{(\varepsilon + p)e^{\nu/2}}{2} \times \\ & \times \left\{ (1 - e^\lambda Q)H_0 + (r^2 \omega^2 e^{-\nu} + n_l + 1)H_1 \right. \\ & + (3e^\lambda Q - 1)K - \frac{4(n_l + 1)e^\lambda Q}{r^2}V \\ & \left. - 2 \left[\omega^2 e^{\lambda/2 - \nu} + 4\pi(\varepsilon + p)e^{\lambda/2} - r^2 \frac{d}{dr} \left(\frac{e^{\lambda/2}Q}{r^3} \right) \right] W \right\}, \quad (36) \end{aligned}$$

where c_{ad}^2 is the adiabatic sound speed of NS matter under oscillations. In this work, we approximate this speed of sound with the equilibrium sound speed $c_{\text{eq}}^2 = dp/d\varepsilon$.

Perturbations at the center of the star $r = 0$ are subject to the boundary conditions $X(R) = 0$, $W(0) = 1$, and

$$\begin{aligned} X(0) = & (\varepsilon_0 + p_0)e^{\nu_0/2} \\ & \left\{ \left[\frac{4\pi}{3}(\varepsilon_0 + 3p_0) - \frac{\omega^2}{l}e^{-\nu_0} \right] W(0) + \frac{K(0)}{2} \right\}, \quad (37) \end{aligned}$$

$$H_1(0) = \frac{lK(0) + 8\pi(\varepsilon_0 + p_0)W(0)}{n_l + 1}. \quad (38)$$

The final boundary condition is derived by solving two trial solutions with $K(0) = \pm(\varepsilon_0 + p_0)$ and then forming a linear combination to satisfy the condition $X(r = R) = 0$, which ensures there are no pressure variations at the surface. By design, $H_0(0) = K(0)$.

At the star's surface, small arbitrary values are assigned to the functions H_1 , K , and W , and backward integration is performed until reaching the point where forward integration from the star's center ends. The forward and backward solutions are then matched at this point. The quasinormal mode frequency for the star is determined by solving the Zerilli equation,

$$\frac{d^2 Z}{dr^{*2}} = [V_Z(r) - \omega^2]Z. \quad (39)$$

The Zerilli function, as expressed in Eq. (20) of [25], depends solely on the perturbation variables H_1 and K , since the fluid perturbations W , V , and X vanish outside

the star. The value $Z(r)$ at the star's surface is determined using the values of H_1 and K at the surface. Beyond the star, Eq. (39) is numerically integrated starting from the surface and extending outward to a distance corresponding to $r = 25 \omega^{-1}$ [25]. The value of Z at $r = 25 \omega^{-1}$ is matched with the corresponding value obtained from the asymptotic expansion of Z , which is valid far from the neutron star's surface. To account for the imaginary component of ω , which is over a thousand times smaller than its real counterpart, it is essential to maintain a relative error of 10^{-6} in our ODE solver for the variables H_1 , K , W , X , and Z .

III.2. Cowling Approximation

Rather than solving the full set of general relativity equations, the Cowling approximation simplifies the problem by neglecting the back-reaction on the gravitational potential. This means metric perturbations are disregarded, and only fluid perturbations are considered. In order to find mode frequencies, one has to solve the following differential equations [30]:

$$\begin{aligned} \frac{dW(r)}{dr} = & \frac{d\varepsilon}{dp} \left[\omega^2 r^2 e^{\Lambda(r) - 2\phi(r)} V(r) + \frac{d\Phi(r)}{dr} W(r) \right] \\ & - l(l + 1)e^{\Lambda(r)} V(r), \\ \frac{dV(r)}{dr} = & 2 \frac{d\Phi(r)}{dr} V(r) - \frac{1}{r^2} e^{\Lambda(r)} W(r) \quad (40) \end{aligned}$$

where,

$$\frac{d\Phi(r)}{dr} = \frac{-1}{\varepsilon(r) + p(r)} \frac{dp}{dr}. \quad (41)$$

The solution of Eq. (40) with the fixed background metric near the origin behaves as follows:

$$W(r) = Ar^{l+1}, \quad V(r) = -\frac{A}{l}r^l. \quad (42)$$

The vanishing perturbed Lagrangian pressure at the surface will provide another constraint to be included while solving Eq. (40), which is given by,

$$\omega^2 e^{\Lambda(R) - 2\Phi(R)} V(R) + \frac{1}{R^2} \frac{d\Phi(r)}{dr} \Big|_{r=R} W(R) = 0. \quad (43)$$

Eqs. (40) are the eigenvalue equations. Solutions that satisfy the boundary condition given by Eq. (43) are the eigenfrequencies of the star.

IV. NUMERICAL RESULTS AND DISCUSSION

IV.1. Equation of State and Mass-Radius relations

Figure 1 illustrates how pressure varies with energy density (i.e., the EoS) for a neutron star under beta-equilibrium and charge-neutral conditions. The left panel

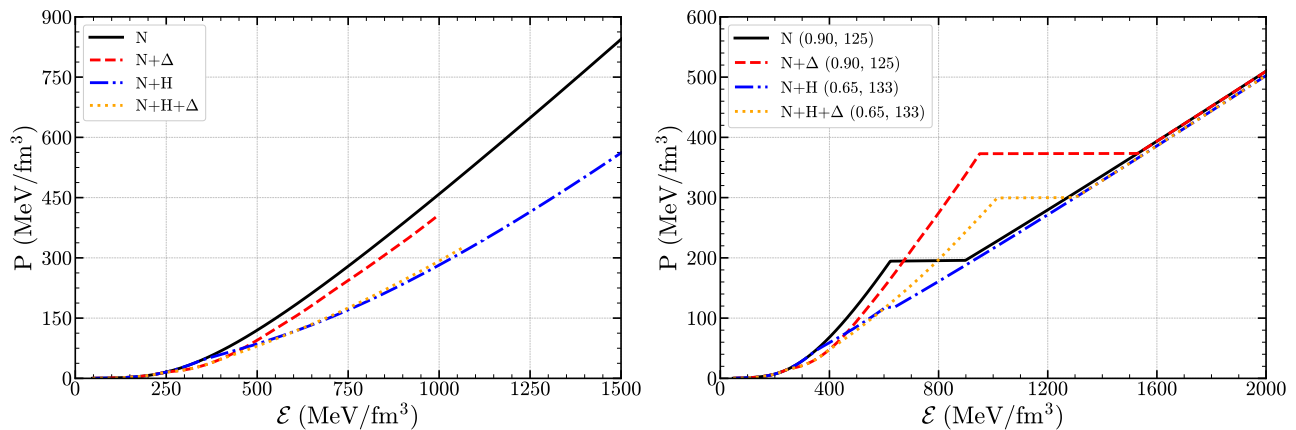


FIG. 1. Energy density and pressure variation for the given DD-ME2 parameter set without (left) and with (right) phase transition to the quark matter at different quark model parameters ($C, D^{1/2}$). The solid line represents the pure nucleonic matter (N) while dashed, dash-dotted, and dotted lines represent the EoS for Δ -admixture nuclear matter $\Delta(N+\Delta)$, with hyperons (N+H), and Δ -admixture hyperonic matter (N+H+ Δ), respectively.

shows different compositions of hadronic matter: pure nucleonic matter (N), Δ -admixture nuclear matter (N+ Δ), with hyperonic matter (N+H), and Δ -admixture hyperonic matter (N+H+ Δ), and the right panel shows the EoS when a phase transition to the quark matter is included. From the left plot, we can see that the pure nucleonic matter results in a stiffer EoS at high densities. The appearance of Δ particles softens the EoS, as additional particle types distribute the Fermi pressure across multiple degrees of freedom. With only nucleons and hyperons present, the EoS softens further, but adding Δ particles to hyperonic matter (N+H+ Δ) introduces complexities. As seen in Figure 1, N+H+ Δ is softer than N+H at low densities but becomes stiffer as density increases. This stiffening occurs because the Δ^- baryon replaces a neutron-electron pair at the Fermi surface, which is energetically favorable due to an attractive potential. Neutral particles, as the Λ and Δ^0 , appear later [81].

Regarding the phase transition, the presence of Δ s causes a shift in the coexistence point towards higher densities for the same deconfined EoS, which is linked to the aforementioned effect. Post-phase transition, the EoS at higher densities is much more uniform compared to its hadronic counterpart. For instance, the parameter set $(C, D^{1/2}) = (0.90, 125 \text{ MeV})$ results in only a slightly stiffer EoS than $(C, D^{1/2}) = (0.65, 133 \text{ MeV})$. However, the position of the coexistence point plays the most crucial role when constructing the hybrid EoS. Thus, for hybrid N+ Δ EoS, the phase transition takes place at a very high density compared to hybrid N+H+ Δ EoS. For the hybrid N+H EoS, the hadron-quark phase transition region is small and occurs at low density compared to the others. This implies a large quark phase present in comparison to the other hybrid EoSs.

Figure 2 depicts the behavior of squared speed of sound as a function of number density for different compositions of the matter studied in this work, without (left) and with (right) phase transition. Thermodynamic stability ensures

that $c_s^2 > 0$ and causality implies an absolute bound $c_s^2 \leq 1$. For very high densities, perturbative QCD findings anticipate an upper limit of $c_s^2 = 1/3$ [82]. The two solar mass requirements, according to several studies [82–84], necessitates a speed of sound squared that exceeds the conformal limit ($c_s^2 = 1/3$), revealing that the matter inside of NS is a highly interacting system. In Figure 2, the c_s^2 for pure nucleonic matter is significantly high, reaching a value of 0.75 at the maximum mass configuration. In the appearance of different particles, one can see the kinks corresponding to the onset of a new particle species, resulting in noticeable changes at the onset of each type. Both pure nucleonic and Δ -mixed nuclear matter exceed the conformal limit. Additionally, the N+H+ Δ EoS shows a higher value of c_s^2 compared to N+H EoS at intermediate densities due to the early emergence of Δ^- particles. For the maximum mass configuration, the c_s^2 for N+H is 0.54 while for N+H+ Δ is 0.51.

When transitioning to quark matter (right plot), c_s^2 exhibits a discontinuity as the density varies abruptly in the interface between the phases. For different particle combinations, kinks are observed before phase transitions, with hybrid N, N+ Δ , and N+H+ Δ EoS violating the conformal limit at low densities. The N+H+ Δ composition predicts a higher c_s^2 due to early Δ^- appearance and delayed quark transition. At high energy densities, all speed of sound values stays well below the conformal limit, unlike previous observations, due to the expected approach of a deconfined EoS towards the conformal limit from below [85]. For all the cases, the speed of sound at the maximum mass configuration lies within the range of 0.25-0.27 because of the transition to the quark matter.

Figure 3 illustrates the mass-radius relationship based on solutions of the TOV equations for various EoSs. The unified EoS employs the Baym-Pethick-Sutherland (BPS) EoS [91] for the outer crust, while the inner crust EoS is generated using the DD-ME2 parameter set in the Thomas-Fermi approximation [92–94]. The left plot represents the MR relations for different compositions of nu-

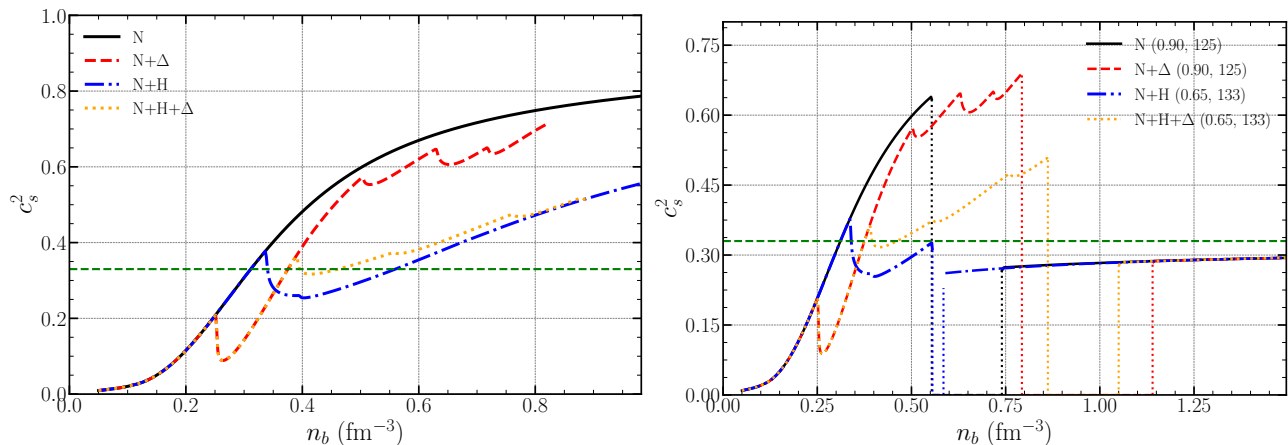


FIG. 2. Speed of sound squared as a function of number density for the different hadronic compositions of EoS without (left) and with phase transition (right) to the quark matter. The dotted lines in the right plot correspond to the mixed-phase region where c_s^2 drops to zero. The green dashed line in both plots represents the conformal limit $c_s^2 = 1/3$.

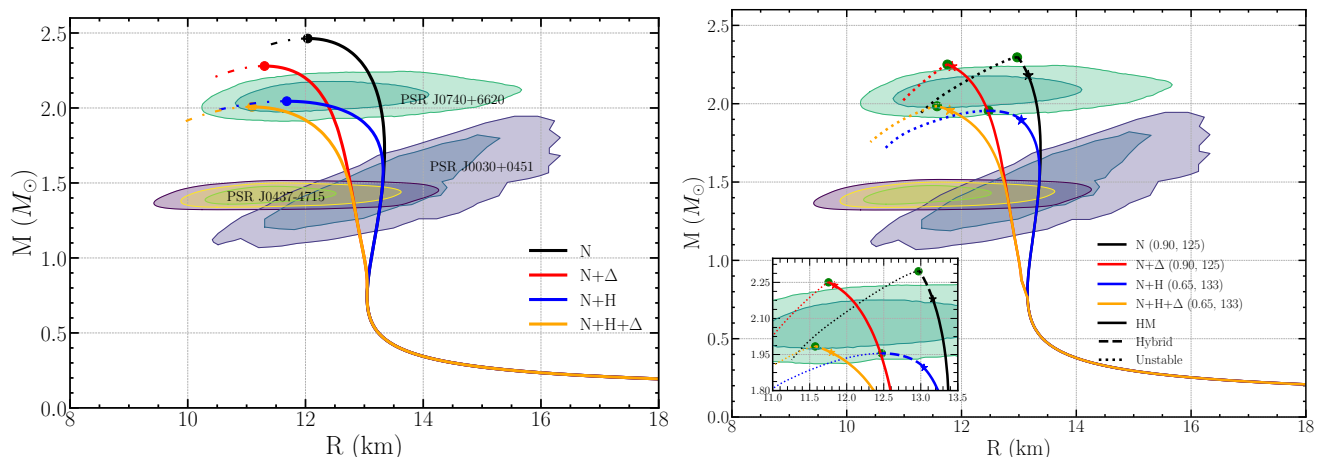


FIG. 3. Left: Mass-Radius relation for the EoS with different hadronic compositions. The solid lines represent the stable part with a solid dot marking the last stable point, hence the maximum mass configuration. The dash-dotted line represents the unstable part. Right: Same as the left plot but with a phase transition to the quark matter. The solid lines represent the hadronic branch. The star symbol corresponds to the beginning of the hybrid stars branch. The solid dot represents the last stable point reached in the center of the maximum-mass solution of the TOV equation. The dotted line represents the unstable part. The various shaded areas are credibility regions from the mass and radius inferred from the analysis of PSR J0740+6620, PSR J0030+0451, and PSR J0437-4715 [86–90].

clear matter without a phase transition. In contrast, the right plot represents the hybrid EoS with the same compositions of nuclear matter but with a phase transition to the quark matter. From the left plot, for purely nucleonic matter, the maximum mass reaches $2.46 M_\odot$ with a radius of 12.04 km. When Δ baryons are included, both the maximum mass and corresponding radius decrease to $2.28 M_\odot$ and 11.30 km. The presence of hyperons softens the EoS, reducing the maximum mass to $2.04 M_\odot$ with a radius of 11.68 km. For hyperonic matter with Δ -admixture, the EoS predicts a maximum mass of $2.00 M_\odot$ and a radius of 11.08 km. All these MR relations satisfy the mass constraints from PSR J0740-220 and several radius constraints from NICER measurements [86–89], including the recent one for PSR J0437-4715 [90]. The solid dot

represents the last stable point reached in the center of the maximum-mass solution of the TOV equation. The dashed line after the solid dot corresponds to the unstable part.

The right plot shows the EoS with a phase transition. The solid lines correspond to the hadronic matter followed by a branch of hybrid stars, represented by dashed lines. The star symbol marks the hadron-quark phase transition point. The solid dot represents the last stable point reached in the center of the maximum-mass solution of the TOV equation. The inset shows a zoomed plot version at around the maximum mass. For the hybrid EoS with nucleons only, the maximum mass is $2.29 M_\odot$ with a radius of 13.02 km. Since the phase transition to the quark matter occurs at high density, a small part of the

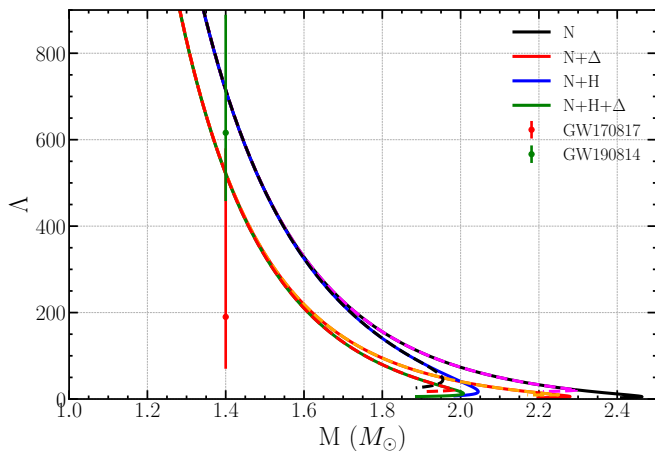


FIG. 4. Dimensionless tidal deformability as a function of M for the EoS studied: without (left) and with (right) phase transition to the quark matter at different quark model parameters ($C, D^{1/2}$). Solid (Dashed) lines correspond to the EoS without (with) a phase transition to the quark matter. The red line represents the constraint on dimensionless tidal deformability at $1.4 M_\odot$ from GW170817 measurement, $\Lambda = 190_{-120}^{+390}$ [2], while as the green line represents the constraint on dimensionless tidal deformability at $1.4 M_\odot$ from GW190814 measurement, $\Lambda = 616_{-158}^{+273}$ if the secondary component is an NS [95].

MR relation presents hybrid stars before it reaches the unstable branch. Including delta baryons soften the EoS and hence the maximum mass decreases to $2.25 M_\odot$ only and the radius to 11.81 km, thereby representing a very small hybrid stars branch. The radius at the canonical mass, $R_{1.4}$ is 13.47 km for nucleons and 12.97 km for nucleons with delta baryons. So while the maximum decreases by around $0.17 M_\odot$ for nucleonic only EoS when phase transition is considered, this decrease is very small for N+ Δ EoS, $\approx 0.05 M_\odot$. This is because deltas appear at a very high density and the phase transition takes place at a much higher density, allowing for a very small amount of quark matter in the core compared to the pure nucleonic hybrid EoS.

For the hybrid EoS with nucleons and hyperons, the maximum mass is $1.95 M_\odot$ with a radius of 12.54 km. We have a substantial amount of pure quark phase here, as the phase transition point is at low density in comparison to all other EoSs. Adding delta baryons slightly increases the maximum mass to $1.98 M_\odot$ because of the delayed phase transition, with a smaller radius of 11.63 km. The MR profiles satisfy the $2.0 M_\odot$ threshold and other constraints. The hybrid nuclear EoS with and without deltas, N and N+H+ Δ , satisfy the $2.0 M_\odot$ limit of PSR J0740+6620. Despite selecting quark parameters for a stiff EoS, including hyperons and a phase transition to quark matter leads to an EoS that softens enough to limit the star’s maximum mass to slightly under $2 M_\odot$, but satisfies the 1σ constraint from PSR J0740+6620.

Figure 4 shows the dimensionless tidal deformability as a function of mass for the different compositions of the EoS studied without (solid) and with (dashed) phase tran-

sition. The red and green lines represent the constraints on the dimensionless tidal deformability at $1.4 M_\odot$ from GW measurements GW170817 and GW190814, respectively $\Lambda = 190_{-120}^{+390}$ [2] and $\Lambda = 616_{-158}^{+273}$, if the secondary component is an NS [95]. For both the nucleon-only EoS and the nucleon-hyperon EoS, the MR relation remains unchanged at $1.4 M_\odot$, and the EoS including hyperons and delta resonances (N+ Δ and N+H+ Δ) behave similarly. These characteristics are also observed when considering the hadron-quark phase transition in these EoSs. The similarity between the curves is attributed to the density-sensitive appearance of hyperons, deltas, and/or deconfinement transition, which occur only in the densest regions near the star’s core. Since the core represents a relatively small portion of the star’s total volume, and tidal deformability is primarily influenced by the outer layers of the object, these exotic compositions have little effect on the star’s response to external tidal forces (see [96] and references therein for further discussion). Hence the dimensionless tidal deformability goes to around 712 for N and N+H EoS with and without phase transition, satisfying the limit from GW190814. For other EoS, N+ Δ and N+H+ Δ , this value decreases to around 520 which is well below the limit from GW170817. All the stellar properties for the EoS without and with phase transition are presented in Table III.

IV.2. f -mode frequency: GR vs Cowling

Figure 5 displays the f -mode frequencies as a function of neutron star mass. The top plot displays various compositions without phase transitions, including pure nucleonic matter, nucleonic matter with hyperons, and delta baryons. The bottom plot shows the same compositions but with a phase transition to quark matter, characterized by different quark model parameters. Dashed lines represent the Cowling approximation in both plots, while solid lines correspond to the full General Relativity framework calculations. The f -mode frequency at the maximum mass configuration for pure nucleonic EoS is 2.12 kHz within the GR framework and 2.37 kHz with the Cowling approximation. The corresponding frequencies at the canonical mass configuration of $1.4 M_\odot$ are 1.61 and 2.05 kHz for GR and Cowling, respectively. This frequency increases at the maximum mass configuration when other exotic particles such as hyperons and deltas appear in the EoS. This behavior is seen in all the cases for GR and Cowling, without and with phase transition. The Cowling approximation overestimates the f -mode frequencies, with errors ranging from 10% to 30%, which decrease as mass increases. For instance, in the case of pure nucleonic matter, the relative error decreases from 27% at $1.4 M_\odot$ to 11.93% at the maximum mass of $2.45 M_\odot$. This behavior is seen in all the EoSs without and with phase transition, showing the effect of how different methods calculate the f -mode frequency with a large difference in the values at low or intermediate masses, which then decreases to higher or maximum mass configurations. The relative er-

TABLE III. Stellar properties for different compositions of EoS: maximum mass (M_{\max}), radius at maximum mass (R_{\max}), at $2.0 M_{\odot}$ ($R_{2.0}$), and at $1.4 M_{\odot}$ ($R_{1.4}$). Dimensionless tidal deformability at $1.4 M_{\odot}$ ($\Lambda_{1.4}$), and speed of sound squared at maximum mass configuration ($c_{s,max}^{2*}$). The upper four rows correspond to the EoS without a phase transition while the lower rows with a phase transition.

Composition	M_{\max} (M_{\odot})	R_{\max} (km)	$R_{2.0}$ (km)	$R_{1.4}$ (km)	$\Lambda_{1.4}$	$c_{s,max}^{2*}$
N	2.46	12.04	13.28	13.28	712.75	0.75
N+ Δ	2.28	11.30	12.40	12.81	522.47	0.71
N+H	2.04	11.68	12.52	13.28	712.75	0.54
N+H+ Δ	2.00	11.08	11.37	12.80	515.25	0.51
N (0.90,1.25)	2.29	13.02	13.38	13.47	712.97	0.27
N+ Δ (0.90,1.25)	2.25	11.81	12.48	12.97	522.65	0.27
N+H (0.65,133)	1.95	12.54	-	13.47	712.97	0.25
N+H+ Δ (0.65,133)	1.98	11.63	-	12.97	515.44	0.25

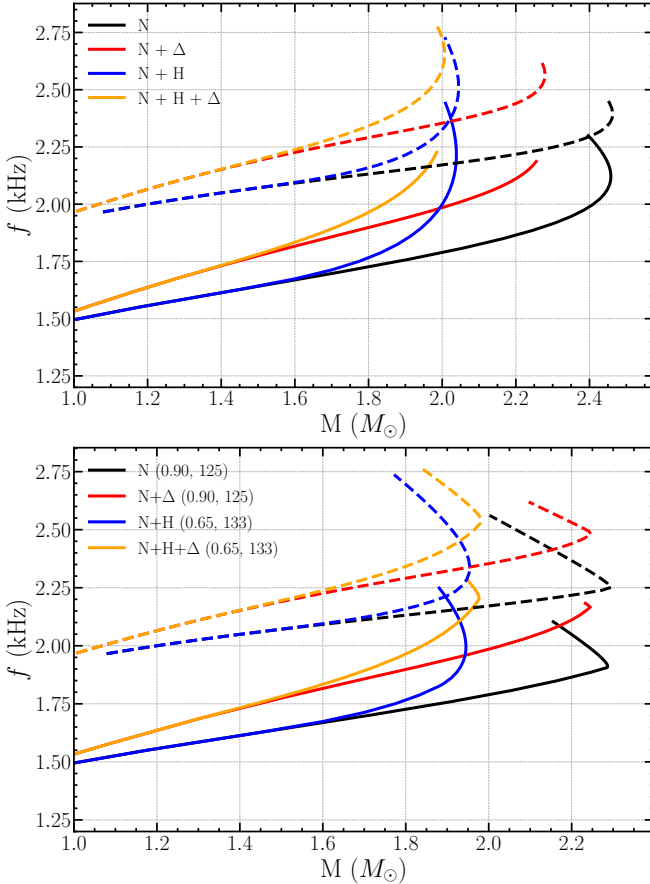


FIG. 5. Mass vs fundamental frequency of non-radial oscillation modes for EoS with different hadronic compositions. Solid lines represent results from the full general relativistic treatment, while dashed lines correspond to the Cowling approximation. The top panel shows compositions with only hadronic matter, and the bottom panel shows compositions with phase transition to the quark matter for different quark model parameters ($C, D^{1/2}$).

rors for other compositions, both with and without phase transitions, are summarized in Table IV. The results are in good agreement with those obtained in [25, 31, 37].

Using GW frequencies to distinguish different EoS families can be effective by considering variations with

TABLE IV. Comparison between the fundamental frequencies (in kHz) calculated using GR (f_{GR}) and Cowling approximation (f_{cow}), at $1.40 M_{\odot}$, $1.80 M_{\odot}$, and at the maximum mass without and with phase transition. The percentage error (P. E.) between GR and Cowling is also shown.

Composition	Mass	f_{GR}	f_{cow}	P. E. (%)
N	1.40	1.6130	2.0491	27.03
	1.80	1.7266	2.1317	23.46
	2.46	2.1205	2.3734	11.93
N+ Δ	1.40	1.7312	2.1520	24.31
	1.80	1.8980	2.2908	20.70
	2.28	2.1865	2.4915	13.95
N+H	1.40	1.6133	2.0491	27.01
	1.80	1.7666	2.1593	22.23
	2.04	2.2043	2.4811	12.56
N+H+ Δ	1.40	1.7328	2.1529	24.24
	1.80	1.9644	2.3419	19.22
	2.00	2.2269	2.5422	14.16
N (0.90,1.25)	1.40	1.6130	2.0491	27.03
	1.80	1.7266	2.1317	23.46
	2.29	1.9110	2.2441	17.43
N+ Δ (0.90,1.25)	1.40	1.7300	2.1520	24.39
	1.80	1.8980	2.2908	20.70
	2.25	2.1662	2.4876	14.84
N+H (0.65,133)	1.40	1.6133	2.0491	27.01
	1.80	1.7666	2.1599	22.27
	1.95	2.0018	2.3166	15.73
N+H+ Δ (0.65,133)	1.40	1.7329	2.1529	24.24
	1.80	1.9648	2.3422	19.21
	1.98	2.2018	2.5225	14.57

star compactness, which can be independently assessed through gravitational redshift measurements from spectral line observations [17, 26, 97, 98]. In Figure 6 we show the variation of f -mode frequencies as a function of stellar compactness. The left plot corresponds to the EoSs without a phase transition whereas the right plot is with phase transition. Solid lines in both panels reflect full general relativistic treatment while the dashed line corresponds to Cowling approximation. Just as in Figure 5, we see an overestimation of frequencies by the Cowling approximation.

Besides the basic properties such as mass, radius, and compactness, dimensionless tidal deformability serves as a crucial observable for constraining the NS EoS. In a

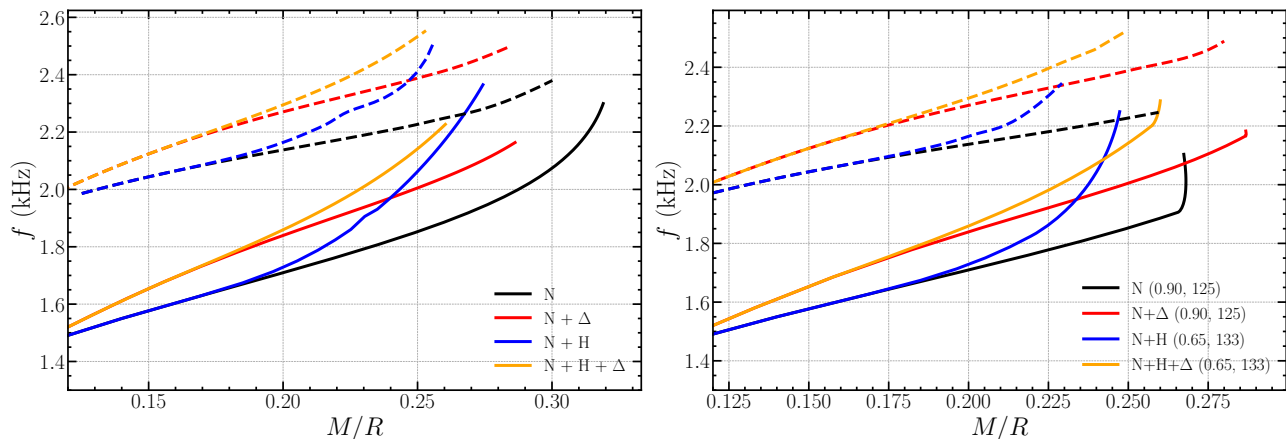


FIG. 6. Left: Stellar compactness (M/R) vs fundamental frequency of non-radial oscillation modes for EoS with different hadronic compositions. Solid lines represent results from the full general relativistic treatment, while dashed lines correspond to the Cowling approximation. Right: Same plots as left plot, but with phase transition to the quark matter at different quark model parameters ($C, D^{1/2}$).

binary system's inspiral phase, NSs exert significant gravitational forces on each other, and the degree of deformation depends on their EoSs. By separately measuring the f -mode frequency and tidal deformability, we obtain insightful data that enhances our understanding of NSs internal structure. Figure 7 illustrates the relationship between f -mode frequencies and the dimensionless tidal deformability. Our results for the f -mode frequency lie well within the limits obtained from the GW170817 observation which is estimated between 1.43 kHz and 2.90 kHz for the more massive NS and between 1.48 kHz and 3.18 kHz for the less massive one.

V. GRAVITATIONAL WAVE ASTEROSEISMOLOGY

V.1. Fitting

Neutron star asteroseismology aims to connect the oscillation modes' angular frequencies and GW damping timescales to the star's core properties, including mass, radius, and rotational frequency. By using inverse asteroseismology, it is possible to derive relationships that are largely independent of the specific EoS. This approach leverages GW observations in combination with the star's global properties – particularly its rotational frequency, which plays a crucial role in rapidly rotating neutron stars – to infer internal structure and dynamics. The concept of GW asteroseismology was initially introduced by Andersson and Kokkotas [97] for certain polytropic EoSs and later explored for some realistic EoSs [26]. They derived an empirical asteroseismology relation between f -mode frequency as a function of average density of the star, namely,

$$f(\text{kHz}) = a + b\sqrt{\frac{\bar{M}}{\bar{R}^3}}, \quad (44)$$

in terms of the dimensionless parameters $\bar{M} = \frac{M}{1.4 M_\odot}$ and $\bar{R} = \frac{R}{10 \text{ km}}$. This was further probed with some EoSs containing exotic phases such as hyperons and quarks by Benhar *et al.* [17]. More studies with exotic phases, quarks, and dark matter were also carried out in Ref. [33, 99–102]. But no work in the context of Δ baryons has been carried out for the f -mode frequency, especially with a hadron-quark phase transition considered.

In Figures 8 and 9, we present the empirical asteroseismology relation for f -mode frequencies as a function of the average density of the star, respectively for the scenarios without and with a phase transition. The upper panels present fitting relations based on the Cowling approximation, while the lower panels display results from the full GR framework. Dot-dashed lines represent fits from previous studies [17, 26, 101–103], and the dotted line corresponds to the fit obtained from our work. All the different values of a and b for the above-fit relation are shown in Table V. For the Cowling approximation fit, the values of a and b from our fit are 1.32 and 1.18 kHz, respectively, without a phase transition, and 1.29 and 1.22 kHz, with a phase transition. They are named Our Fit 1 (Cowling) and Our Fit 2 (Cowling) for without and with phase transition, respectively. Unlike earlier works, our results differ significantly from previous studies because we included Δ baryons in our analysis. This consideration alters the equation of state, leading to the observed variations in the fit relations. For the GR fit, the values of a and b are 0.44 and 1.72 kHz, respectively, without phase transition, and 0.39 and 1.79 kHz with phase transition. They are named Our Fit 1 (GR) and Our Fit 2 (GR) for without and with phase transition, respectively.

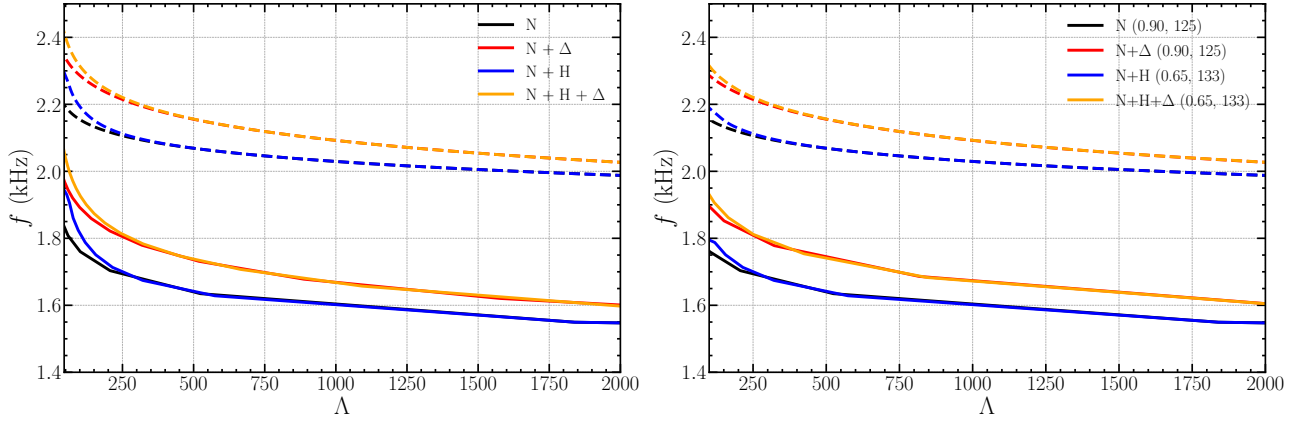


FIG. 7. Left: Dimensionless tidal deformability vs fundamental frequency of non-radial oscillation modes for EoS with different hadronic compositions. Solid lines represent results from the full general relativistic treatment, while dashed lines correspond to the Cowling approximation. Right: Same plots as left plot, but with phase transition to the quark matter at different quark model parameters ($C, D^{1/2}$).

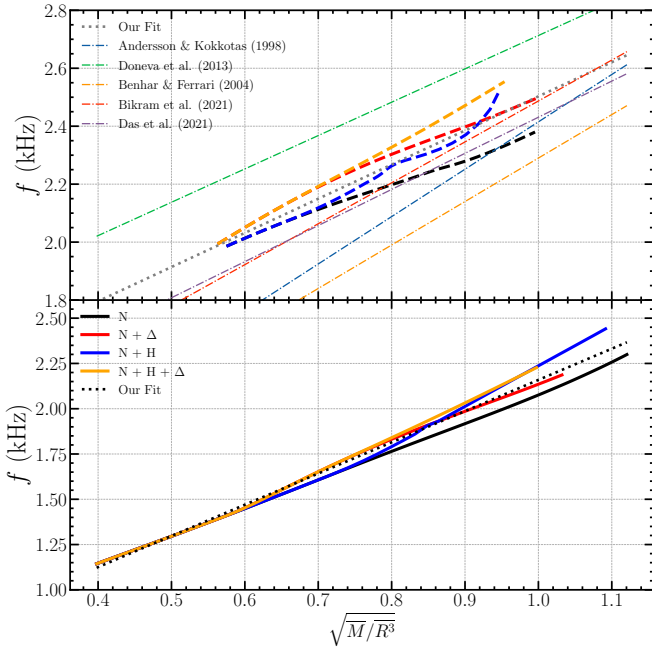


FIG. 8. Average density of the star vs fundamental frequency of non-radial oscillation modes for EoS with different hadronic compositions. The lower (upper) plot represents results from the full general relativistic (Cowling) treatment. The dot-dashed lines in the upper plot correspond to the fits from various studies whereas the dotted line corresponds to the fit from our work.

V.2. Universal relations

The relationships between different mode frequencies, when normalized by the mass or radius of a neutron star, reveal a significant connection to stellar compactness. These relations appear almost unaffected by the choice of the EoS. Prior research on g -modes has discovered a universal relation between mass-scaled angular frequency,

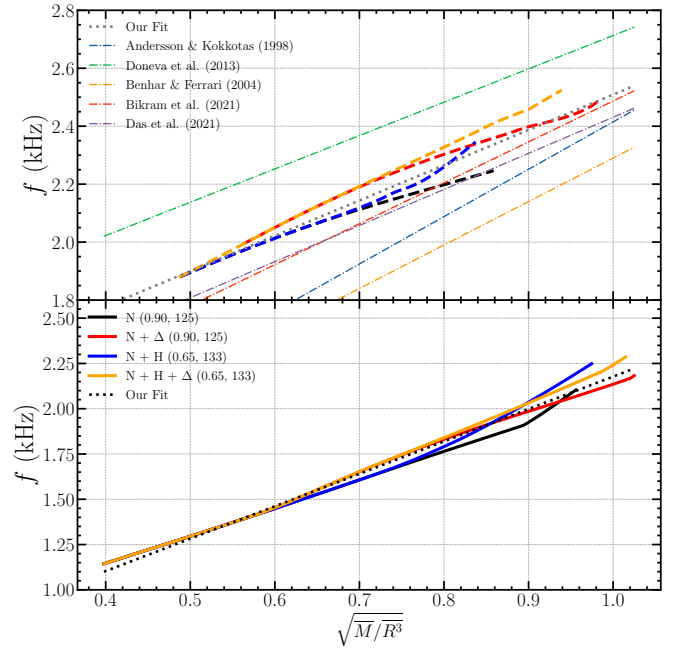


FIG. 9. Same as Figure 8, but with phase transition to the quark matter at different quark model parameters ($C, D^{1/2}$).

TABLE V. Values of fitting coefficients a and b in kHz for Eq. 44 from different works and our results.

Reference	a (kHz)	b (kHz)
Benhar <i>et al.</i> [17]	0.79	1.500
Andersson and Kokkotas [26]	0.78	1.635
Das <i>et al.</i> [101]	1.185	1.246
Pradhan and Chatterjee [102]	1.075	1.412
Doneva <i>et al.</i> [103]	1.562	1.151
Our Fit 1 (Cowling)	1.32	1.18
Our Fit 1 (GR)	0.44	1.72
Our Fit 2 (Cowling)	1.29	1.22
Our Fit 2 (GR)	0.39	1.79

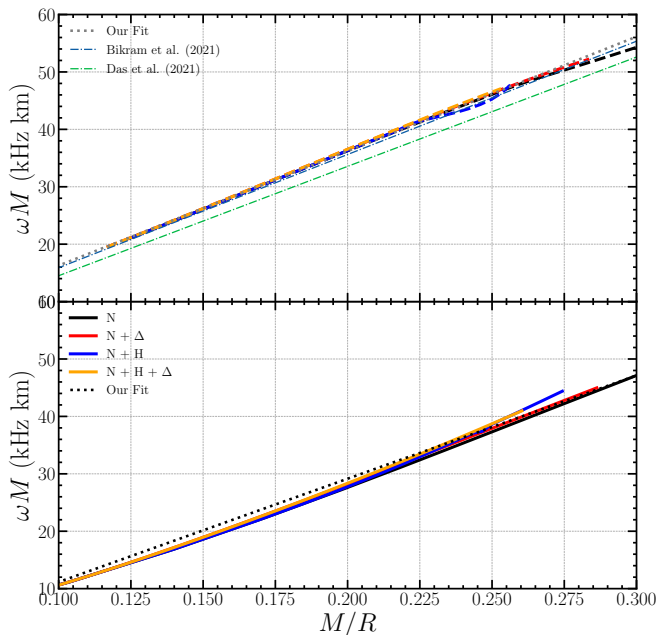


FIG. 10. Stellar compactness vs the angular frequency ($\omega = 2\pi f$) scaled by mass (ωM) for EoS with different hadronic compositions. The lower (upper) plot represents results from the full general relativistic (Cowling) treatment. The dot-dashed lines in the upper plot correspond to the fits from various studies whereas the dotted line in both the upper and lower plot corresponds to the fit from our work.

ωM , and the compactness, M/R [104]. In this study, we investigate these relationships considering hyperons, Δ baryons, and their combination, highlighting how the mass and radius-scaled angular frequency vary with stellar compactness.

In Figures 10 and 11, we plot mass-scaled angular frequency (ωM) as a function of stellar compactness. The left plot represents the analysis without a phase transition, whereas the right panel has a phase transition. The lower (upper) plot represents the full general relativistic (Cowling) treatment results. The universal relation between ωM and M/R is given by

$$\omega M = a \left(\frac{M}{R} \right) - b, \quad (45)$$

where a and b are fitting coefficients in kHz km.

In the upper plot, dot-dashed lines represent fits from various studies, while the dotted line in both upper and lower plots corresponds to the fit derived from our work. Although the fit from Pradhan and Chatterjee [102] matches very closely to our fit, the one from Das *et al.* [101] differs.

In the Cowling approximation, the parameters a and b are 199.40 and -3.66 kHz km, respectively, for cases without phase transition, and 200 and -3.88 with phase transition. For the full GR fit, the values of a and b are set to 179.61 and -6.63 without phase transition, and 180.65 and -6.92 when phase transition is considered.

Figures 12 and 13 illustrate the relationship between ωR (the product of the f -mode frequency ω and radius

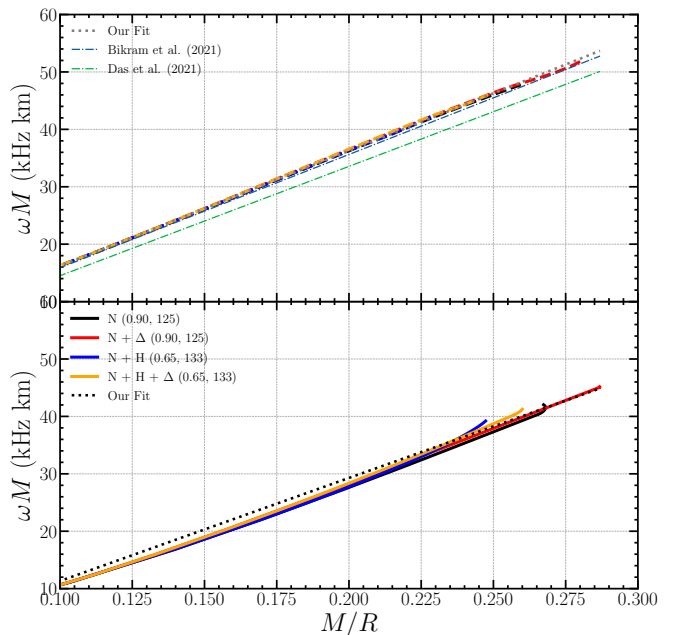


FIG. 11. Same as Figure 10, but with phase transition to the quark matter at different quark model parameters ($C, D^{1/2}$).

R) and the compactness (M/R), respectively without and with a hadron-quark deconfinement transition. The universal relation takes the same form as Eq. (45),

$$\omega R = a \left(\frac{M}{R} \right) + b. \quad (46)$$

The lower panels depict results obtained from full GR calculations, which account for both fluid and gravitational perturbations, providing the most accurate theoretical predictions. In contrast, the upper panels show results under the Cowling approximation, where gravitational perturbations are neglected. This simplification leads to an overestimation of ωR , evident from the consistently higher values compared to the GR results. The overestimation is more pronounced at lower compactness and reduces as compactness increases, reflecting the stronger coupling of surface fluid perturbations to the tidal field in more compact stars. The dotted line in both panels corresponds to the universal fit derived from the current study. In the upper panel, the dot-dashed line represents the fit from the previous study by Das *et al.* [101], providing a comparative reference. In the Cowling approximation, the parameters a and b (in kHz km) are 114.54 and 157.36, respectively, for cases without a phase transition and 145.93 and 151.15 with a phase transition.

For the full GR fit, the values of a and b (in kHz km) are set to 286.57 and 78.50 without phase transition, and 307.54 and 75.12 when phase transition is considered. However, the correlation is slightly weaker in the case of ωR with M/R .

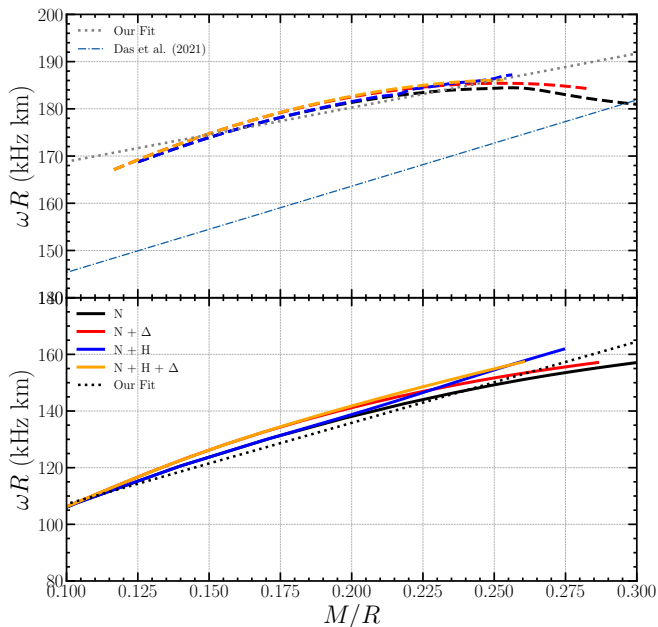


FIG. 12. Same as Figure 10 but angular frequency scaled by radius (ωR) as function of compactness.

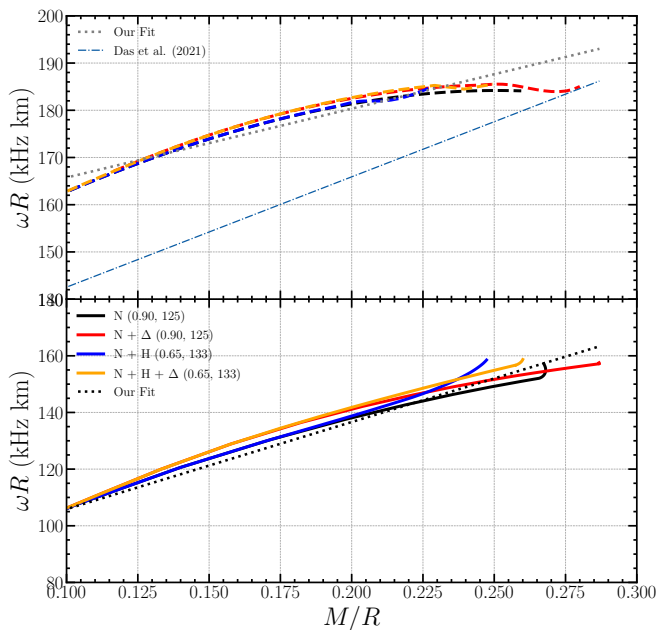


FIG. 13. Same as Figure 11 but angular frequency scaled by radius (ωR) as function of compactness.

VI. SUMMARY AND CONCLUSION

In this work, we explored the impact of hyperons and delta baryons on the non-radial f -mode oscillations of neutron stars, both with and without a hadron-quark transition. Our analysis employed the Cowling approximation and a fully general relativistic (GR) framework to compute f -mode oscillation frequencies and compare the results. The Equation of State (EoS) for hadronic matter

was constructed using the density-dependent relativistic mean-field (DD-RMF) model, which reliably reproduces nuclear matter properties at saturation density and complies with astrophysical constraints. Specifically, we used the DDME2 parameter set to create four EoSs representing different compositions: nucleons only, nucleons with hyperons, nucleons with delta baryons, and nucleons with both hyperons and delta baryons. To extend the study, we included phase transitions to quark matter, parameterized by a density-dependent quark mass (DDQM) model. The quark model parameters were carefully selected to remain consistent with astrophysical observations. For constructing hybrid EoSs, we employed the Maxwell treatment for the phase transition. This comprehensive approach allowed us to investigate how the inclusion of hyperons, delta baryons, and quark matter influences f -mode oscillations and their astrophysical implications.

For the EoS without a phase transition, the speed of sound at the last stable configuration reaches 0.75 for the pure nucleonic case. This value decreases with the inclusion of hyperons and Δ baryons, as these particles soften the EoS. For the EoS with a phase transition, the speed of sound at the last stable point (maximum mass configuration) falls within the hybrid stars phase, ranging from 0.25 to 0.27, which is significantly below the conformal limit. Solving the TOV equations, we obtain a pure nucleonic neutron star with a maximum mass of $2.46 M_{\odot}$ and a corresponding radius of 12.04 km. The presence of hyperons and Δ baryons softens the EoS and hence the maximum mass decreases to a value of $2.00 M_{\odot}$ for N+H+ Δ case. With the phase transition to the quark matter, the MR relations decrease to lower values. The amount of hybrid stars phase is very small in the case of pure nucleonic hybrid EoS. Because deltas have a high density and the phase transition occurs at a much greater density, the core of the hybrid stars formed contains a very small amount of quark matter compared to the nucleonic hybrid EoS. For the hybrid EoS with nucleons and hyperons only, we see a larger fraction of the hybrid stars phase.

We studied the f -mode frequencies as a function of stellar mass for all the cases using both Cowling as well as GR framework. We observed that the Cowling approximation overestimates the f -mode frequencies, with errors ranging from 10-30%, which decreases with the increasing maximum mass. This large difference in the values of the frequency at the maximum mass is also evident when there is a phase transition to the quark matter. For better understanding, we also examined the f -mode frequencies as a function of compactness and dimensionless tidal deformability, showing that these frequencies align well with constraints from gravitational wave observations, such as GW170817, for more massive and less massive NSs. Universal relations connecting f -mode frequencies to average density, compactness, and tidal deformability were derived and compared to previous works. The inclusion of Δ baryons in the EoS significantly influenced these relations, distinguishing the results from earlier studies.

Empirical fitting relations for f -mode frequencies were

provided for both Cowling and GR frameworks, understanding the impact of phase transitions and demonstrating variations from prior studies due to the inclusion of additional degrees of freedom in the EoS. Additionally, relationships involving mass-scaled angular frequencies (ωM) and scaled frequencies (ωR) with compactness (M/R) were analyzed, showing overestimations under the Cowling approximation and stronger coupling of perturbations in more compact stars under GR.

This work comprehensively analyzes f -mode oscillations in neutron stars across a range of EoS scenarios, including phase transitions to quark matter. The results underscore the importance of full GR calculations over the Cowling approximation, especially for accurately modeling oscillation frequencies in less compact configurations. By exploring the interplay between f -mode frequencies, tidal deformability, and compactness, the study demonstrates the potential of gravitational wave observations to constrain neutron star EoSs and internal structures effectively.

The inclusion of exotic particles like Δ baryons, along with the derived universal relations, significantly enhances our understanding of the complex behavior of neutron stars under diverse physical conditions. These particles play a crucial role in softening the EoS, influencing the star's maximum mass, radius, and oscillation properties. The presence of exotic baryons, which emerge at high densities, also impacts the phase transition to quark matter, shedding light on the intricate interplay between hadronic and quark phases in the cores of neutron stars.

These findings not only align with current observational constraints, such as the measured maximum masses and

radii of neutron stars but also provide a robust framework for future research. In particular, they offer valuable insights into neutron star asteroseismology, helping to connect oscillation modes and damping timescales with the star's internal composition and structure. Moreover, the results have profound implications for interpreting gravitational wave data, enabling more accurate modeling of neutron star mergers and their post-merger remnants.

By integrating theoretical predictions with observational data, our studies aim to contribute to a deeper understanding of dense matter physics. They also highlight the importance of exotic particles in advancing our knowledge of the QCD phase diagram and the fundamental properties of compact objects, contributing to the broader goal of unifying the knowledge of nuclear physics, astrophysics, and gravitational wave astronomy in a unified theoretical approach.

VII. ACKNOWLEDGEMENT

P.T. sincerely thanks Tuhin Malik for his invaluable support in enhancing the accuracy and robustness of the code utilized in this work. This work is a part of the project INCT-FNA proc. No. 464898/2014-5. It is also supported by Conselho Nacional de Desenvolvimento Científico e Tecnológico (CNPq) under Grants No. 307255/2023-9 (O. L.), and 401565/2023-8 (Universal, O. L.). I.A.R. acknowledges support from the Alexander von Humboldt Foundation. K.D.M. thanks financial support from the São Paulo State Research Foundation (FAPESP), under Grant No. 2024/01623-6.

-
- [1] B. P. Abbott and R. Abbott *et al.*, *Phys. Rev. Lett.* **119**, 161101 (2017).
 - [2] B. P. Abbott and R. Abbott *et al.*, *Phys. Rev. Lett.* **121**, 161101 (2018).
 - [3] B. P. Abbott *et al.* (LIGO Scientific, Virgo), *Astrophys. J. Lett.* **892**, L3 (2020), arXiv:2001.01761 [astro-ph.HE].
 - [4] B. Sathyaprakash *et al.*, *Bull. Am. Astron. Soc* **51**, 251 (2019).
 - [5] M. Punturo *et al.*, *Classical and Quantum Gravity* **27**, 194002 (2010).
 - [6] V. Kalogera *et al.*, arXiv e-prints, arXiv:2111.06990 (2021), arXiv:2111.06990 [gr-qc].
 - [7] I. Bombaci, in *Proceedings of the 12th International Conference on Hypernuclear and Strange Particle Physics (HYP2015)* (2017) p. 101002.
 - [8] H. Xiang and G. Hua, *Phys. Rev. C* **67**, 038801 (2003).
 - [9] J. J. Li, A. Sedrakian, and F. Weber, *Physics Letters B* **783**, 234–240 (2018).
 - [10] G. Malfatti, M. G. Orsaria, I. F. Ranea-Sandoval, G. A. Contrera, and F. Weber, *Phys. Rev. D* **102**, 063008 (2020).
 - [11] C. D. Capano, I. Tews, S. M. Brown, B. Margalit, S. De, S. Kumar, D. A. Brown, B. Krishnan, and S. Reddy, *Nature Astronomy* **4**, 625–632 (2020).
 - [12] D. Gondek, P. Haensel, and J. L. Zdunik, *A&A* **325**, 217–227 (1997).
 - [13] A. Passamonti, M. Bruni, L. Gualtieri, A. Nagar, and C. F. Sopuerta, *Phys. Rev. D* **73**, 084010 (2006).
 - [14] A. Passamonti, N. Stergioulas, and A. Nagar, *Phys. Rev. D* **75**, 084038 (2007).
 - [15] C. Chirenti, M. C. Miller, T. Strohmayer, and J. Camp, *The Astrophys. J. Lett.* **884**, L16 (2019).
 - [16] K. D. Kokkotas and B. G. Schmidt, *Living Rev. Rel.* **2**, 2 (1999), arXiv:gr-qc/9909058.
 - [17] O. Benhar, V. Ferrari, and L. Gualtieri, *Phys. Rev. D* **70**, 124015 (2004), arXiv:astro-ph/0407529.
 - [18] B. P. Abbott *et al.* (LIGO Scientific Collaboration and Virgo Collaboration), *Phys. Rev. Lett.* **122**, 061104 (2019).
 - [19] R. Abbott *et al.*, *Prog. Th. Exp. Phys.* **2022** (2022), 10.1093/ptep/ptac073.
 - [20] V. Ferrari, G. Miniutti, and J. A. Pons, *Mon. Not. Roy. Astron. Soc.* **342**, 629 (2003), arXiv:astro-ph/0210581.
 - [21] P. C. Mock and P. C. Joss, *The Astrophysical Journal* **500**, 374 (1998).
 - [22] K. D. Kokkotas, T. A. Apostolatos, and N. Andersson, *Mon. Not. Roy. Astron. Soc.* **320**, 307–315 (2001), arXiv:gr-qc/9901072.
 - [23] B. P. Abbott *et al.* (LIGO Scientific, Virgo), *Astrophys. J.* **874**, 163 (2019), arXiv:1902.01557 [astro-ph.HE].
 - [24] R. Abbott *et al.* (LIGO Scientific, Virgo, KAGRA, VIRGO), *Astrophys. J.* **966**, 137 (2024),

- arXiv:2210.10931 [astro-ph.HE].
- [25] A. Kunjipurayil, T. Zhao, B. Kumar, B. K. Agrawal, and M. Prakash, *Phys. Rev. D* **106**, 063005 (2022), arXiv:2205.02081 [nucl-th].
- [26] N. Andersson and K. D. Kokkotas, *Mon. Not. Roy. Astron. Soc.* **299**, 1059–1068 (1998), arXiv:gr-qc/9711088.
- [27] H. K. Lau, P. T. Leung, and L. M. Lin, *Astrophys. J.* **714**, 1234–1238 (2010), arXiv:0911.0131 [gr-qc].
- [28] T. K. Chan, Y.-H. Sham, P. T. Leung, and L.-M. Lin, *Phys. Rev. D* **90**, 124023 (2014).
- [29] T. Zhao and J. M. Lattimer, *Phys. Rev. D* **106**, 123002 (2022), arXiv:2204.03037 [astro-ph.HE].
- [30] B. K. Pradhan and D. Chatterjee, *Phys. Rev. C* **103**, 035810 (2021), arXiv:2011.02204 [astro-ph.HE].
- [31] D. G. Roy, T. Malik, S. Bhattacharya, and S. Banik, *Astrophys. J.* **968**, 124 (2024), arXiv:2312.02061 [astro-ph.HE].
- [32] R. Maiti and D. Chatterjee, (2024), arXiv:2412.04373 [astro-ph.HE].
- [33] I. F. Ranea-Sandoval, O. M. Guilera, M. Mariani, and M. G. Orsaria, *JCAP* **12**, 031 (2018), arXiv:1807.02166 [astro-ph.HE].
- [34] H. C. Das, A. Kumar, S. K. Biswal, and S. K. Patra, *Phys. Rev. D* **104**, 123006 (2021), arXiv:2109.01851 [nucl-th].
- [35] P. Thakur, T. Malik, A. Das, T. K. Jha, B. K. Sharma, and C. Providência, (2024), arXiv:2408.03780 [nucl-th].
- [36] D. Dey, J. A. Pattnaik, R. N. Panda, M. Bhuyan, and S. K. Patra, (2024), arXiv:2412.06739 [astro-ph.HE].
- [37] B. K. Pradhan, D. Chatterjee, M. Lanoye, and P. Jaikumar, *Phys. Rev. C* **106**, 015805 (2022), arXiv:2203.03141 [astro-ph.HE].
- [38] N. Barman, B. K. Pradhan, and D. Chatterjee, (2024), arXiv:2408.00739 [astro-ph.HE].
- [39] I. A. Rather, K. D. Marquez, G. Panotopoulos, and I. Lopes, *Phys. Rev. D* **107**, 123022 (2023), arXiv:2303.11006 [nucl-th].
- [40] I. A. Rather, K. D. Marquez, B. C. Backes, G. Panotopoulos, and I. Lopes, *JCAP* **05**, 130 (2024), arXiv:2401.07789 [nucl-th].
- [41] H.-B. Li, Y. Gao, L. Shao, R.-X. Xu, and R. Xu, *MNRAS* **516**, 6172–6179 (2022).
- [42] Kokkotas, K. D. and Ruoff, J., *A&A* **366**, 565–572 (2001).
- [43] S. Sen, S. Kumar, A. Kunjipurayi, P. Routaray, T. Zhao, and B. Kumar, (2022), arXiv:2205.02076 [nucl-th].
- [44] V. Sagun, G. Panotopoulos, and I. Lopes, *Phys. Rev. D* **101**, 063025 (2020).
- [45] G. Panotopoulos and I. Lopes, *Phys. Rev. D* **98**, 083001 (2018).
- [46] P. Routaray, H. C. Das, S. Sen, B. Kumar, G. Panotopoulos, and T. Zhao, (2022), arXiv:2211.12808 [nucl-th].
- [47] M. Dutra, O. Lourenço, S. Avancini, B. Carlson, A. Delfino, D. Menezes, C. Providência, S. Typel, and J. Stone, *Physical Review C* **90**, 055203 (2014).
- [48] O. Lourenço, M. Dutra, C. H. Lenzi, C. V. Flores, and D. P. Menezes, *Physical Review C* **99**, 045202 (2019).
- [49] T. Malik, M. Ferreira, B. K. Agrawal, and C. Providência, *Astrophys. J.* **930**, 17 (2022).
- [50] M. G. de Paoli, D. P. Menezes, L. B. Castro, and C. C. Barros, Jr, *J. Phys. G* **40**, 055007 (2013), arXiv:1207.4063 [math-ph].
- [51] M. Oertel, M. Hempel, T. Klähn, and S. Typel, *Rev. Mod. Phys.* **89**, 015007 (2017).
- [52] R. Brockmann and H. Toki, *Phys. Rev. Lett.* **68**, 3408–3411 (1992).
- [53] G. A. Lalazissis, T. Nikšić, D. Vretenar, and P. Ring, *Phys. Rev. C* **71**, 024312 (2005).
- [54] L. L. Lopes, K. D. Marquez, and D. P. Menezes, *Physical Review D* **107**, 036011 (2023).
- [55] A. Issifu, K. D. Marquez, M. R. Pelicer, and D. P. Menezes, (2023), arXiv:2302.04364 [nucl-th].
- [56] S. Typel and H. H. Wolter, *Nucl. Phys. A* **656**, 331–364 (1999).
- [57] C. Fuchs, H. Lenske, and H. H. Wolter, *Phys. Rev. C* **52**, 3043–3060 (1995).
- [58] C. J. Xia, G. X. Peng, S. W. Chen, Z. Y. Lu, and J. F. Xu, *Phys. Rev. D* **89**, 105027 (2014).
- [59] B. C. Backes, K. D. Marquez, and D. P. Menezes, *The European Physical Journal A* **57**, 1–9 (2021).
- [60] A. R. Bodmer, *Physical Review D* **4**, 1601–1606 (1971).
- [61] E. Witten, *Physical Review D* **30**, 272–285 (1984).
- [62] B. C. Backes, E. Hafemann, I. Marzola, and D. P. Menezes, *Journal of Physics G: Nuclear and Particle Physics* **48**, 055104 (2021).
- [63] K. Nagata, *Prog. Part. Nucl. Phys.* **127**, 103991 (2022), arXiv:2108.12423 [hep-lat].
- [64] Y. Aoki, G. Endrodi, Z. Fodor, S. D. Katz, and K. K. Szabo, *Nature* **443**, 675–678 (2006), arXiv:hep-lat/0611014.
- [65] X. Luo, S. Shi, N. Xu, and Y. Zhang, *Particles* **3**, 278–307 (2020), arXiv:2004.00789 [nucl-ex].
- [66] A. Bazavov *et al.*, *Phys. Rev. D* **95**, 054504 (2017), arXiv:1701.04325 [hep-lat].
- [67] A. Bazavov *et al.* (HotQCD), *Phys. Rev. D* **96**, 074510 (2017), arXiv:1708.04897 [hep-lat].
- [68] K. Fukushima and T. Hatsuda, *Rept. Prog. Phys.* **74**, 014001 (2011), arXiv:1005.4814 [hep-ph].
- [69] D. N. Voskresensky, M. Yasuhira, and T. Tatsumi, *Nucl. Phys. A* **723**, 291–339 (2003), arXiv:nucl-th/0208067.
- [70] T. Maruyama, S. Chiba, H.-J. Schulze, and T. Tatsumi, *Phys. Rev. D* **76**, 123015 (2007), arXiv:0708.3277 [nucl-th].
- [71] M. B. Pinto, V. Koch, and J. Randrup, *Phys. Rev. C* **86**, 025203 (2012), arXiv:1207.5186 [hep-ph].
- [72] G. Lugones, A. G. Grunfeld, and M. Al Ajmi, *Phys. Rev. C* **88**, 045803 (2013), arXiv:1308.1452 [hep-ph].
- [73] G. Lugones and A. G. Grunfeld, *Phys. Rev. C* **95**, 015804 (2017), arXiv:1610.05875 [nucl-th].
- [74] G. Lugones and A. G. Grunfeld, *Phys. Rev. C* **99**, 035804 (2019), arXiv:1811.09954 [astro-ph.HE].
- [75] R. C. Tolman, *Phys. Rev.* **55**, 364–373 (1939).
- [76] J. R. Oppenheimer and G. M. Volkoff, *Phys. Rev.* **55**, 374–381 (1939).
- [77] G. Chanmugam, *Astrophys. J.* **217**, 799–808 (1977).
- [78] F. J. Zerilli, *Phys. Rev. Lett.* **24**, 737–738 (1970).
- [79] L. Lindblom and S. L. Detweiler, *Astrophys. J. Suppl.* **53**, 73–92 (1983).
- [80] S. L. Detweiler and L. Lindblom, *Astrophys. J.* **292**, 12–15 (1985).
- [81] K. D. Marquez, D. P. Menezes, H. Pais, and C. m. c. Providência, *Phys. Rev. C* **106**, 055801 (2022).
- [82] P. Bedaque and A. W. Steiner, *Phys. Rev. Lett.* **114**, 031103 (2015).
- [83] C. C. Moustakidis, T. Gaitanos, C. Margaritis, and G. A. Lalazissis, *Phys. Rev. C* **95**, 045801 (2017).
- [84] I. Tews, J. Carlson, S. Gandolfi, and S. Reddy, *The Astrophys. J.* **860**, 149 (2018).

- [85] P. Bedaque and A. W. Steiner, *Phys. Rev. Lett.* **114**, 031103 (2015), arXiv:1408.5116 [nucl-th].
- [86] M. C. Miller *et al.*, *The Astrophysical Journal Letters* **918**, L28 (2021).
- [87] T. E. Riley *et al.*, *The Astrophysical Journal Letters* **918**, L27 (2021).
- [88] M. C. Miller *et al.*, *Astrophys. J.* **887**, L24 (2019).
- [89] T. E. Riley *et al.*, *Astrophys. J.* **887**, L21 (2019).
- [90] D. Choudhury, T. Salmi, S. Vinciguerra, T. E. Riley, Y. Kini, A. L. Watts, B. Dorsman, S. Bogdanov, S. Guillot, P. S. Ray, D. J. Reardon, R. A. Remillard, A. V. Bilous, D. Huppenkothen, J. M. Lattimer, N. Rutherford, Z. Arzoumanian, K. C. Gendreau, S. M. Morsink, and W. C. G. Ho, *The Astrophysical Journal Letters* **971**, L20 (2024).
- [91] G. Baym, C. Pethick, and P. Sutherland, *Astrophys. J.* **170**, 299–317 (1971).
- [92] S. S. Avancini, L. Brito, J. R. Marinelli, D. P. Menezes, M. M. W. de Moraes, C. Providência, and A. M. Santos, *Phys. Rev. C* **79**, 035804 (2009).
- [93] H. Pais and C. m. c. Providência, *Phys. Rev. C* **94**, 015808 (2016).
- [94] I. A. Rather, A. Usmani, and S. Patra, *Nuclear Physics A* **1010**, 122189 (2021).
- [95] R. Abbott *et al.* (LIGO Scientific, Virgo), *Astrophys. J. Lett.* **896**, L44 (2020).
- [96] B. Kumar, S. K. Biswal, and S. K. Patra, *Phys. Rev. C* **95**, 015801 (2017).
- [97] N. Andersson and K. D. Kokkotas, *Phys. Rev. Lett.* **77**, 4134–4137 (1996), arXiv:gr-qc/9610035.
- [98] N. K. Glendenning, *Compact stars: Nuclear physics, particle physics, and general relativity* (1997).
- [99] J. L. Blázquez-Salcedo, L. M. González-Romero, and F. Navarro-Lérida, *Phys. Rev. D* **89**, 044006 (2014), arXiv:1307.1063 [gr-qc].
- [100] S. Shirke, B. K. Pradhan, D. Chatterjee, L. Sagunski, and J. Schaffner-Bielich, *Phys. Rev. D* **110**, 063025 (2024), arXiv:2403.18740 [gr-qc].
- [101] H. C. Das, A. Kumar, S. K. Biswal, and S. K. Patra, *Phys. Rev. D* **104**, 123006 (2021).
- [102] B. K. Pradhan and D. Chatterjee, *Phys. Rev. C* **103**, 035810 (2021).
- [103] D. D. Doneva, E. Gaertig, K. D. Kokkotas, and C. Krüger, *Phys. Rev. D* **88**, 044052 (2013), arXiv:1305.7197 [astro-ph.SR].
- [104] H. Sotani, N. Yasutake, T. Maruyama, and T. Tatsumi, *Physical Review D* **83** (2011), 10.1103/physrevd.83.024014.